

RESEARCH ARTICLE

10.1002/2014JA020427

Key Points:

- A beam 0.1 A of 5 MeV electrons in 1 μ s will produce detectable signatures
- Signatures include ionization, optical emissions, X-rays, and backscatter
- Variations with beam energy and divergence are used to find the optimal beam

Correspondence to:

R. A. Marshall,
ram80@stanford.edu

Citation:

Marshall, R. A., M. Nicolls, E. Sanchez, N. G. Lehtinen, and J. Neilson (2014), Diagnostics of an artificial relativistic electron beam interacting with the atmosphere, *J. Geophys. Res. Space Physics*, 119, 8560–8577, doi:10.1002/2014JA020427.

Received 23 JUL 2014

Accepted 19 SEP 2014

Accepted article online 23 SEP 2014

Published online 10 OCT 2014

Diagnostics of an artificial relativistic electron beam interacting with the atmosphere

R. A. Marshall¹, M. Nicolls², E. Sanchez², N. G. Lehtinen³, and J. Neilson⁴
¹Department of Aeronautics and Astronautics, Stanford University, Stanford, California, USA, ²Center for Geospace Sciences, SRI International, Menlo Park, California, USA, ³Department of Electrical Engineering, Stanford University, Stanford, California, USA, ⁴SLAC National Accelerator Laboratory, Menlo Park, California, USA

Abstract We use a Monte Carlo model to simulate the interaction of a beam of relativistic (0.5–10 MeV) electrons with the upper atmosphere as they are injected downward from a notional high-altitude (thermospheric/ionospheric) injection platform. The beam parameters, defined by realistic parameters of a compact linear accelerator, are used to create a distribution of thousands of electrons. Each electron is injected downward from 300 km altitude toward the dense atmosphere, where it undergoes elastic and inelastic collisions, leading to secondary ionization, optical emissions, and X-rays via bremsstrahlung. In this report we describe the model initialization (i.e., development of the electron distribution), essential features of the Monte Carlo model, and secondary outputs, including optical emissions, X-ray fluxes, secondary ionization, and backscattered energetic electron fluxes. Optical emissions are propagated to the ground through the lower atmosphere, including the effects of atmospheric absorption and scattering, to estimate the brightness of the emission column for a given beam current and energy. Similarly, X-ray fluxes are propagated to hypothetical detectors on balloons and satellites. Secondary ionization is used to estimate the radar signal returns from various ground-based radar facilities. Finally, simulated backscattered electron fluxes are measured at the injection location. The simulation results show that each of these diagnostics should be readily detectable by appropriate instruments.

1. Introduction

We are interested in the use of a beam of relativistic electrons (0.5–10 MeV) for space science applications. A beam of relativistic electrons, injected from a balloon, rocket, or spacecraft could be used for field line tracing in the magnetosphere during geomagnetic substorm events, beam-particle interactions and the generation and amplification of whistler mode waves in the radiation belts, and atmospheric electrification and the initiation of upper atmospheric electric discharges.

Energetic electron beams with energies in the tens of keV range were used for some of these applications in the 1970s and 1980s [e.g., Winckler, 1980]. The largest space experiments involving keV beams were all flown on the space shuttle. The STS-3 mission included an electron source of 1 keV electrons up to 100 mA current, and also flew the Iowa plasma diagnostics package [e.g., Neupert *et al.*, 1982]. The Space Experiments with Particle Accelerators (SEPAC) experiment on the ATLAS-1 mission [e.g., Burch *et al.*, 1993] included a 6.25 keV electron beam of up to 1.2 A current. The Tethered Satellite System (TSS)-1 and TSS-1R missions [Stone and Bonifazi, 1998] included a 100 mA, 1 keV beam emitted by the Fast Pulse Electron Gun, which was used to investigate ionospheric currents produced by an injected beam.

The application of MeV electron beams in space has been of interest since the late 1980s [Banks *et al.*, 1987, 1990]; a comprehensive review of MeV electron beam research up to 1992 was provided by Neupert and Banks [1992]. However, none have yet been flown. Considerable past work has been undertaken to model the effects of relativistic beams.

Following on the initial studies of Banks *et al.* [1987, 1990], Neupert *et al.* [1996] provided the first detailed modeling of a 5 MeV beam interacting with the upper atmosphere between 40 and 60 km altitude using a Monte Carlo simulation approach. They calculated electron density perturbations and conductivity changes, and proposed that the experiment could be used to study the electrification of the upper atmosphere and chemical reaction paths in this altitude range. After the discovery of sprites and gigantic jets,

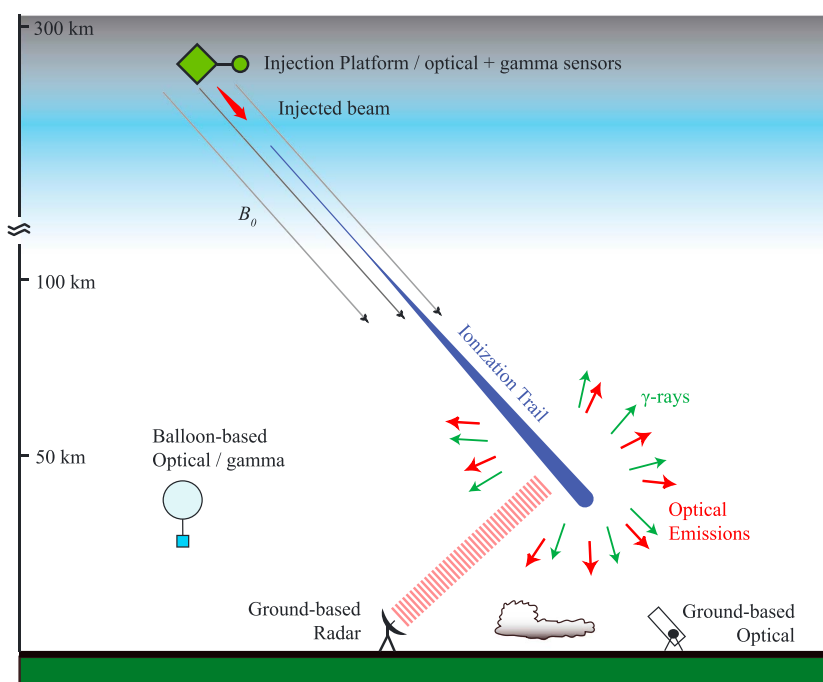


Figure 1. Beam Injection scenario. A pulse of electrons (or series of pulses) is injected from a satellite, rocket, or high-altitude balloon. Ionization is produced in the atmosphere between ~ 40 and 100 km altitude, as are optical emissions, X-rays, and gamma rays. These signatures may be measured from radar (ionization), ground-based optical, or balloon-borne optical and X-ray sensors. In addition, the injection platform itself may be outfitted with sensors to detect optical emissions, X-rays, and backscattered electrons.

Neubert and Gilchrist [2004] went on to investigate the application of MeV beams in triggering upward lightning above thunderstorms.

Detailed calculations of the ionospheric perturbation were presented in Krause [1998], this time using beam envelope equations rather than a full Monte Carlo simulation. The results of Krause [1998] will be used in the present work to compare results of the beam propagation in the atmosphere. Neubert and Gilchrist [2002] simulated relativistic electron beam injection from a spacecraft using 3-D particle-in-cell simulations and found stable injection and propagation of relativistic beams with currents several orders of magnitude higher than for keV beams. Therein it was found that MeV beams are more stable than keV beams thanks to the higher relativistic electron mass, lower beam density, and reduced effects of spacecraft charging.

Apart from direct measurements of beam electrons and VLF waves in situ, diagnostics of the electron beam for each of these applications rely on the beam-atmosphere interaction. Relativistic electrons impinging on the increasingly dense atmosphere from above create secondary ionization, which may be detected by ground-based radar or VLF subionospheric remote sensing. In addition, beam electrons and secondary ionization lead to excitation of neutral species, which upon relaxation emit visible photons; in essence, this is a high-energy aurora (auroral electrons are typically 1–10 keV, but the ionization and optical emission processes are the same). Such optical emissions were measured during the SEPAC keV beam experiment Neubert *et al.* [1995]. Relativistic electrons also undergo bremsstrahlung, emitting high-energy photons (X-rays and gamma rays) as they are decelerated by molecular nuclei. While a negligible X-ray flux will reach the ground, they may be detectable from high-altitude balloons, rockets, or spacecraft, including the same platform as the particle accelerator. (For simplicity, in this paper we will refer to all high-energy photons as X-rays.) The beam injection, atmospheric interactions, and detection scenarios are sketched in Figure 1.

In this paper, we describe the method by which we calculate each of these diagnostics (secondary ionization, optical emissions, X-rays, and backscattered electrons) from a known injected beam. We vary beam parameters including the beam current, electron energy and energy spread, and pulse time. Our beam-atmosphere simulation method is centered around a Monte Carlo model of electron propagation

Table 1. Realistic Beam Parameters for COMPASS Instrument; Used as Range of Parameters for Simulations

Parameter	Minimum	Typical	Maximum	Units
Beam current I_0	0.01	0.1	1	Amperes
Beam energy E	0.5	2	10	MeV
Beam divergence $\langle \theta^2 \rangle$	0.005 ²	0.01 ²	0.5 ²	radians ²
Energy spread ΔE (σ)		± 5		%
Pulse time τ	0.1	1	10	μ s

through a gas, developed by *Lehtinen et al.* [1999], and referred to as the Stanford Monte Carlo (SMC) model. We describe the essential features of this model in section 3. First, we show how the input distribution of electrons is generated from beam parameters.

2. Beam Parameters

The input to the SMC model is a distribution of relativistic electrons, specified with initial position components q_x , q_y , and q_z and momentum components p_x , p_y , and p_z . We generate this electron distribution based on realistic beam parameters for the Compact Particle Accelerator for Space Science (COMPASS) instrument, under preliminary design by SLAC National Accelerator Laboratory and SRI International. These beam parameters are shown in Table 1.

Since the total number of electrons injected is finite and both spatially and temporally confined, we generate a beam pulse with realistic spatial and temporal distributions, but a much smaller number of particles; for example, we may use 100,000 electrons in the SMC model to represent the 6.25×10^{11} electrons in a 0.1 A, 1 μ s pulse. The outputs can then simply be scaled by the ratio of these two numbers.

The beam divergence $\langle \theta^2 \rangle$ (also related to beam emittance) is the mean-squared pitch angle that the beam makes with respect to the nominal beam direction; the square root of this number (which we denote θ) represents the angle that is one standard deviation away from the center of the angle distribution.

2.1. Beam Radius

While the total ionization events, and thus photons and X-rays, are not sensitive to the beam shape, knowledge of the beam cross section (i.e., beam radius) is important for accurate estimate of the *density* of new ionization, on which the radar backscatter signal depends. An initial equilibrium beam radius can be determined from the parameters in Table 1 if the paraxial approximation is used, i.e., the electron parallel velocity is much greater than the perpendicular velocity, $v_{\parallel} \gg v_{\perp}$. This is generally true for beam current $I_0 \ll I_A$, where I_A is the Alfvén current:

$$I_A = \beta \gamma \left(\frac{4\pi\epsilon_0 m_0 c^3}{q_e} \right) \simeq 17 \beta \gamma \text{ kA for electrons} \quad (1)$$

For beam currents approaching I_A , the magnetic pinch effect is severe enough to turn the particle trajectories back, breaking the validity of the paraxial approximation. However, in all cases studied here, we use $I_0 \leq 0.1$ A, and the lowest electron energy considered is 500 keV, for which $I_A \simeq 29$ kA; hence, we can assume $I_0 \ll I_A$.

Radial forces acting on the electron beam include (a) magnetic pressure generated by the beam current, (b) focusing from the external magnetic field, and (c) outward pressure associated with the beam's divergence. When these forces are balanced, the beam can achieve an equilibrium radius r_{eq} given by [e.g., *Humphries*, 1990]

$$r_{eq} = \frac{2\beta c}{\omega_{ce}} \sqrt{\langle \theta^2 \rangle + K} \quad (2)$$

where $\langle \theta^2 \rangle$ is the beam divergence, $\omega_{ce} = q_e B_0 / m_e$ is the electron gyrofrequency of the beam magnetic field, and $K \sim I_0 / I_A$ is the beam perveance [e.g., *Krause*, 1998]. When $|K| \ll \langle \theta^2 \rangle$, the equilibrium radius reduces to

$$r_{eq} = \frac{2\beta c}{\omega_{ce}} \sqrt{\langle \theta^2 \rangle} = \frac{2cm_e}{q_e B_0} \theta \beta \gamma = 68.1 \theta \beta \gamma \text{ for } B_0 = 0.5 \text{ Gauss} \quad (3)$$

Table 2. Beam Equilibrium Radius for Given Beam Electron Energies

Electron energy (MeV)	0.5	1	2	5	10	20
β	0.8630	0.9412	0.9791	0.9957	0.9988	0.9997
γ	1.98	2.96	4.92	10.79	20.59	40.17
Beam radius (m)	1.2	2.0	3.4	7.6	14.6	28.6

since $\omega_{ce} = q_e B_0 / \gamma m_e$. Table 2 lists the equilibrium radius for a range of beam electron energies, for a typical magnetic field in the high-latitude ionosphere of 50,000 nT, a beam current of 0.1 A, and a typical root-mean-square divergence of $\theta = 0.01$ radians (0.57°). Note that even for low currents, we use the full equation (2), including the beam perveance, for Table 2 and in our model calculations.

For our calculations, we assume that the beam is injected at its equilibrium radius. While this may not be practical for a realistic injection, the Monte Carlo method does not allow us to consider radial forces from beam electric and magnetic self-fields. However, we find in the simulations that follow that the initial beam radius has very little effect on the resulting diagnostic signatures, because the beam expands to many times this radius upon collision with the dense atmosphere below 100 km altitude.

2.2. Initial Electron Distribution

Given a beam radius $r_b = r_{eq}$ determined above, along with the pulse current I_0 , electron energy E and energy spread ΔE , we generate a distribution of N electrons with weighted random parameters, where N is a large number (on the order of 100,000 electrons). These N electrons each represent N_{tot}/N electrons in the actual pulse, where $N_{tot} = I_0 \tau / q_e$ is the total number of electrons in the pulse, I_0 is the pulse current, and τ is the pulse time. N_{tot} and the electron energy give us a finite amount of input energy, to which outputs can be compared. For a 0.1 A pulse in 1 μ s, $N_{tot} = 6.25 \times 10^{11}$ electrons, independent of the electron energy.

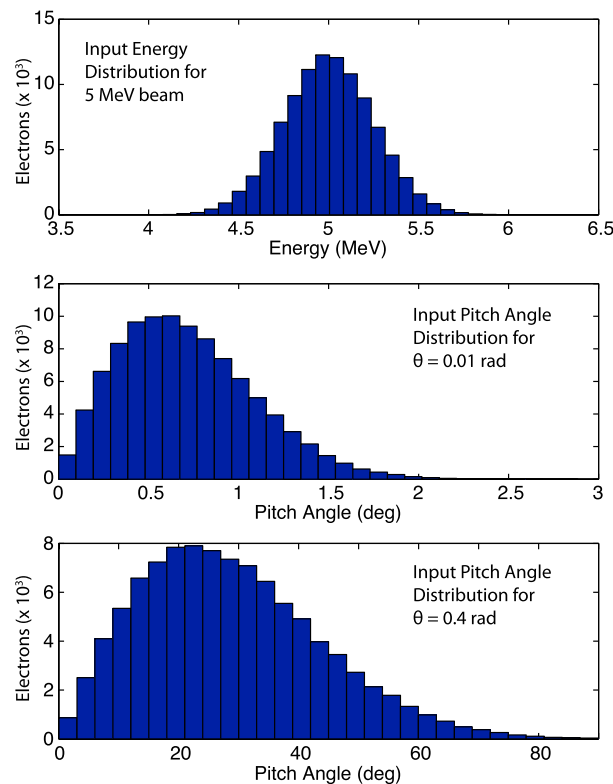


Figure 2. Histograms of the (top) input electron distributions in energy and (middle and bottom) pitch angle for a 5 MeV beam with 5% energy spread and beam divergence angles of 0.01 radians in Figure 2 (middle) and 0.4 radians in Figure 2 (bottom).

1. **Energy.** The electron energy is chosen randomly from a Gaussian distribution centered at E with a standard deviation of $\sigma_E = \Delta E$.
2. **Pitch angle.** The electron pitch angle α is chosen randomly from a 2-D Gaussian distribution centered at zero (i.e., parallel to B_0) with $\sigma_\alpha = \theta$, the square root of the mean-squared divergence angle of the beam.
3. **Gyrophase.** The phase of the electron gyration about the field line ϕ is chosen randomly from the uniform distribution $[0, 2\pi]$.
4. **Position.** The electron initial altitude is chosen to be $q_z = 300$ km. The lateral displacement R from a vertical field line at $x = 0, y = 0$ is chosen randomly from a Gaussian distribution centered at $x = 0, y = 0$, with $\sigma_R = r_b$, the beam radius.

The randomly chosen R and ϕ are then used to determine the initial position coordinates q_x and q_y of the electron, in a coordinate system with vertical B_0 . Representative distributions of electron energy and pitch angle are shown in Figure 2, for a beam energy of 5 MeV,

a beam energy spread of 5%, and beam divergence angles (RMS) of 0.01 and 0.4 radians. These histograms are generated for an input of 10^5 random electrons.

The initial momentum vector components are determined from E and α by assuming a vertical B_0 , so that the $p_\perp = |p| \sin \alpha$ and $p_z = |p| \cos \alpha$. The components p_x and p_y are determined from the random gyrophase ψ of the electron. Finally, the initial position coordinates \mathbf{q} and momentum coordinates \mathbf{p} are rotated by the angle of B_0 in the $y - z$ plane (B_x is assumed to be zero). Rotation of the initial position components does not change the initial positions much compared to the 300 km altitude, but it ensures that the beam cross section is circular in the plane perpendicular to B_0 .

2.3. Model Caveats for Beam Propagation

The use of the SMC model to propagate a beam of electrons into the upper atmosphere from above has a number of model assumptions and inherent shortcomings. Most importantly, the SMC model inherently cannot simulate a “beam,” but rather one electron at a time. As such, any electromagnetic interactions among the beam electrons are ignored. These include the self-generated beam electric and magnetic fields that arise from a nonneutral charge distribution in the beam and a beam current, respectively. In equation (2), the beam magnetic field is a key parameter defining the beam perveance K . In previous work [Krause, 1998], it was assumed that the beam magnetic field is “matched” to the background magnetic field, and so we use the background field B_0 to calculate the beam radius above. The assumptions of charge-neutralized beams with negligible current neutralization are generally valid for the injection scenarios considered here [Krause, 1998]. Beam instabilities, especially ion hose and two-stream [Krause, 1998], may also impact beam propagation, but these are not considered here.

The present treatment of the electron beam furthermore does not consider energy loss and scattering due to excitation of ELF and VLF waves interactions and spacecraft charging [e.g., Neubert *et al.*, 1986; Neubert and Gilchrist, 2002]. Although these effects have been shown to be less pronounced for MeV beams than for keV beams used in the past, they still need to be quantified. Modeling efforts are currently underway.

Mishin and Khazanov [2006] suggest the possibility that during the beam propagation, neutralizing currents must be produced within the ionospheric plasma, but in the low-density region between the E and F region ionosphere layers, these neutralizing currents can become unstable. As such, plasma waves develop which inhibit the beam propagation. These effects will be addressed in later future work and are neglected in the present calculations.

3. Monte Carlo Simulation

The details of the SMC model are described in Lehtinen [2000]. Here we describe a few key features of the model and refer the reader to Lehtinen [2000] for details.

The SMC model tracks a set of test electrons, one at a time, while storing position \mathbf{q} and momentum \mathbf{p} components. The motion of these energetic electrons is described by the Langevin equation,

$$\frac{d\mathbf{p}}{dt} = q_e \mathbf{E} + \frac{q_e}{m\gamma} \mathbf{p} \times \mathbf{B} + \mathbf{\Gamma}(t) \quad (4)$$

where $\mathbf{\Gamma}(t)$ is a stochastic force which accounts for collisions. $\mathbf{\Gamma}(t)$ has two parts, one involving energy loss through the dynamic friction function F_D and the other involving changes in angular momentum through angular diffusion. Both dynamic friction and angular diffusion are treated with analytical expressions given in Lehtinen [2000]. Dynamic friction results in a reduction in the electron energy and deposition of that energy in the ambient atmosphere; the loss of energy per unit distance is directly related to the instantaneous electron energy. In addition, new energetic electrons are produced through collisions; the cross section for this energetic ionization depends on the energies of the incident and newly created electrons.

Angular diffusion is similarly included as a stochastic process. Electrons undergo many scattering events through the atmosphere, but the scattering angle is very small for each event. Small-angle collisions are implemented as random changes to the direction of \mathbf{p} by an angle $\Delta\Theta$.

The inclusion of a background magnetic field in equation (4) has a significant effect on simulation time. In the absence of the background magnetic field, the largest time step possible is related to the frequency of collisions with atmospheric constituents, which is directly related to the atmospheric number density. On the other hand, with B_0 included, the time step is limited by the gyration period, so that the gyromotion of

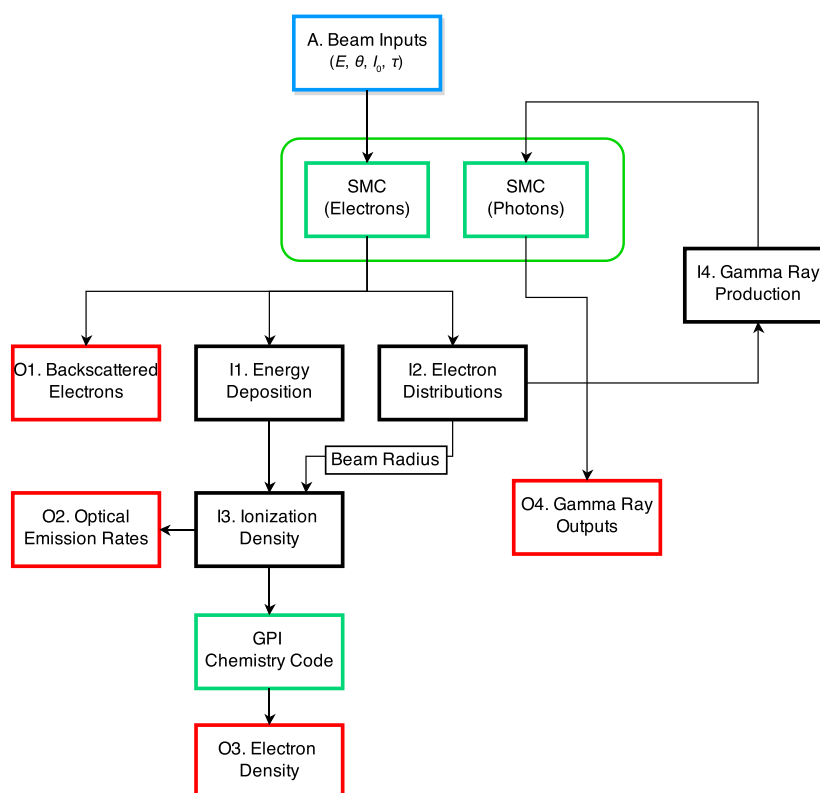


Figure 3. Block diagram of SMC model implementation for beam simulations. Green blocks denote time-dependent model calculations; black boxes denote intermediate outputs; and red boxes denote final diagnostic outputs. See the text for descriptions of each block.

the electrons is properly captured. Given that the electron gyrofrequency is on the order of 1–2 MHz near the Earth's surface, our time steps must be a fraction of a microsecond. Tests comparing simulations with and without the magnetic field have been conducted and show that the magnetic field strongly influences all of the key diagnostics that we calculate in this paper.

4. Example Simulation

In this section we describe how the simulations are run and how the different diagnostic outputs are calculated; along the way we show results for an example simulation, which utilizes a 0.1 A, 0.1 μ s pulse of 5 MeV electrons. We simulate an injection over Poker Flat Research Range north of Fairbanks, AK, at nighttime in winter; this gives us the magnetic field (54,436 nT, 12.5° dip angle) and atmospheric density profile from MSIS-E-90 [Hedin, 1991].

The simulation procedure is outlined in Figure 3. Time-domain simulation codes are shown in green; intermediate outputs in black; and final diagnostic outputs in red. First, from input beam parameters a distribution of electrons is generated as described above (Figure 3, box A). Next, the SMC code is run to propagate electrons through the atmosphere. At regular time intervals, the SMC code outputs (I1) the energy deposition (eV/m/s) as a function of altitude, (I2) the electron distribution (q and p components for all surviving electrons), and (O1) the backscattered electrons distribution (q and p components for all electrons that have “escaped”—to be defined in section 4.3).

4.1. Beam Radius

The SMC code does not store the 3-D locations of energy deposition for each electron, as it would produce prohibitively large arrays. Instead, the energy deposition is output only versus altitude. To extrapolate to a 3-D distribution, we measure the beam radius as a function of altitude as the beam propagates. We use the surviving electron distribution (Figure 3, I2) at each output time step (set so that the beam propagates ~ 1 –2 km per step) and fit a Gaussian distribution, from which the radius is taken as the standard deviation.

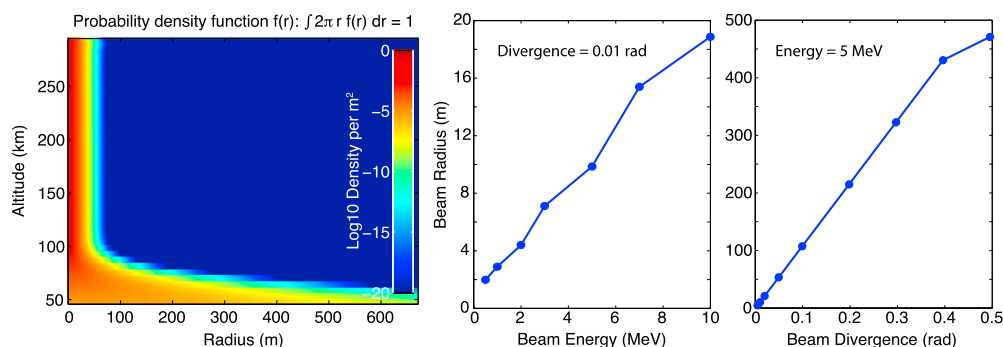


Figure 4. (left) Normalized electron distribution $f(r)$ derived from electron positions at each time (altitude) step in its downward propagation. This function is used to scale the energy deposition from eV/m to eV/m³ at each altitude. (middle) Measured beam radius at 150 km altitude for different input beam energies. (right) Measured beam radius at 150 km altitude for different input beam divergence.

We find that from the injection altitude (say, 300 km) down to the lowest altitude of interest, the electron distribution is fit by a Gaussian with very high accuracy. Since the beam is only 1 μ s in duration, most electrons are confined in a very narrow 300 m altitude range, so this fit can be associated with a single altitude. After the beam is scattered and most surviving electrons begin to propagate back up the field line, the Gaussian fit is poor, but at that point energy deposition is negligible.

Figure 4 (left) shows the normalized distribution of electrons in radial space for the 5 MeV beam. This distribution $f(r)$ is normalized such that the integral $2\pi \int_0^\infty f(r) r dr = 1$ at any given altitude. Thus, the energy deposition profiles in eV/m/s can be multiplied by this distribution to get the 3-D energy deposition in eV/m³/s.

Figure 4 (middle) shows the measured beam radius for different energy beams, as measured from the distribution function in Figure 4 (left) at 150 km altitude, before the beam has begun to increase in size due to collisions. Figure 4 (right) shows the beam radius for different input beam divergence angles (RMS values). These variations will be referred to in section 5 when we vary the input beam energy and divergence to investigate their effects on the diagnostic signatures.

4.2. Ionization and Electron Density

Ionization rates and optical emission rates (Figure 3, I3 and O2) are calculated at each altitude step from the energy deposition profiles that are output by the SMC code. Ionization is calculated under the assumption that every 35 eV of energy deposited produces one ionization pair [Rees, 1963].

From ionization rates in pairs/m³/s, we seek the electron density perturbation (Figure 3, O3) as a function of altitude and time. To calculate ΔN_e , we use a modified form of the Glukhov-Pasko-Inan (GPI) atmospheric chemistry code [Glukhov et al., 1992]. The original GPI model simultaneously solves a set of four ordinary differential equations describing the evolution of electrons, negative ions, positive ions, and positive cluster ions. The code was modified by Lehtinen and Inan [2007] to include negative cluster ions, which are important below ~ 50 km altitude; we refer to this five-species model as GPI5.

We use the full ionization rates as a function of altitude and time as inputs to the GPI5 code and watch the relaxation of the new electron density over ~ 100 ms. Figure 5 shows the electron density versus altitude (left) and versus altitude and time (right). For this 5 MeV beam, we find a peak change in the electron density of 5.5×10^7 m⁻³ at 44 km altitude, and we find that the disturbance recovers over 10–100 ms, faster at lower altitudes. The peak electron density compares very well to Neubert et al. [1996], who found a peak of $\sim 5 \times 10^8$ m⁻³ at 44 km altitude, but for an 80 mA, 10 μ s pulse. Neubert et al. [1996] did not model the recovery of this new ionization.

4.3. Backscattered Electrons

Depending on the beam source conditions and model parameters, a large fraction of the beam electrons can be backscattered into space without completely depositing their energy in the upper atmosphere. Neubert et al. [1990] measured and calculated the “return current” to the injection platform for the Charge

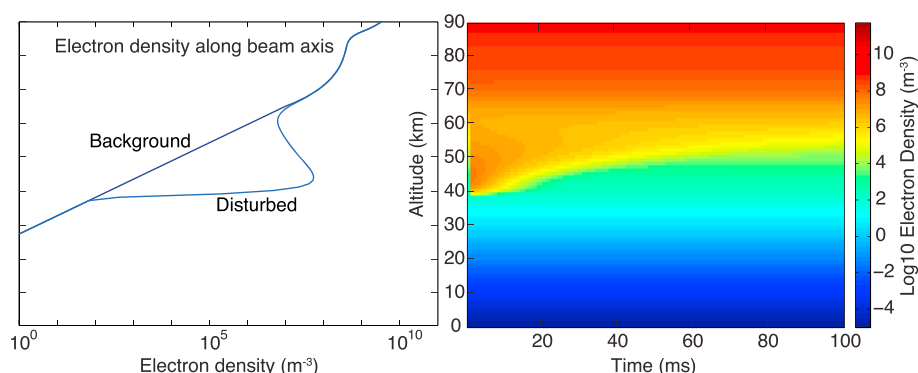


Figure 5. Modified electron density due to 5 MeV, 0.1 A beam injection. (left) The background and peak modified electron density profiles versus altitude; the peak is $\sim 7 \times 10^7$ m⁻³. (right) Time evolution of the electron density disturbance; recovery occurs over 10–100 ms, faster at lower altitudes.

2 platform, emitting 1 keV electrons with a current of 48 mA. Here backscattered electrons were considered to be produced through a beam-atmosphere interaction. The measured and calculated return currents approaching 30% of the beam current, but it was not investigated how this depended on beam parameters such as divergence and energy.

The SMC model considers electrons to be “backscattered” when they reach a set altitude above which the probability of collisions is negligible; this is chosen in all simulations to be 500 km. The backscattered flux is not sensitive to this choice of altitude, since the backscattered electrons are confined by the magnetic field. Figure 6 shows the backscattered electron energy distribution for the 5 MeV, 0.1 A beam. We observe that a significant flux of electrons are backscattered in a very small radius (~ 50 m), since the electrons are confined to the field line. The spectrum of backscattered electrons (Figure 6, middle) shows a soft spectrum from a few keV up to 2 MeV; very few electrons over 1 MeV are scattered back up the field line. The pitch angle distribution (Figure 6, right) shows that the very narrow cone of electrons injected return widely distributed in pitch angle, with very few small pitch angles, none with pitch angles above 70° . Clearly, electrons begin to escape before they can be scattered to low pitch angles; and high-pitch angle electrons are lost to the atmosphere before they can escape.

The backscattered electron flux is likely to be a very good diagnostic tool, due to the large backscattered flux and the ability to measure energy spectra. The flux and spectra measured can be used to infer a great deal about the atmospheric interaction, such as the fraction of beam energy deposited. However, one caveat remains: the backscattered electron beam is very narrow, and the injection platform, whether a rocket or a satellite, will have moved in the time between injection and backscatter. For example, for an injection from 300 km altitude by a satellite, the majority of the backscattered beam reaches the satellite within ~ 10 ms, during which time the satellite will have moved ~ 75 m (assuming a velocity of 7.5 km/s); at that

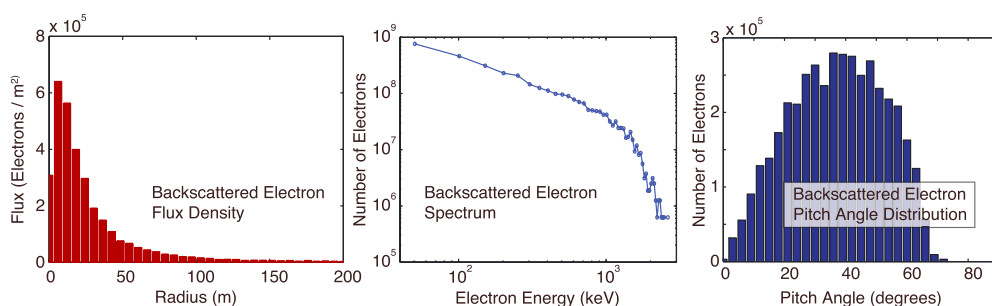


Figure 6. Backscattered electrons, integrated over the duration of the backscattered pulse. (left) Flux of backscattered electrons versus distance from the field line. (middle) Energy spectrum of backscattered electrons. (right) Pitch angle distribution of backscattered electrons.

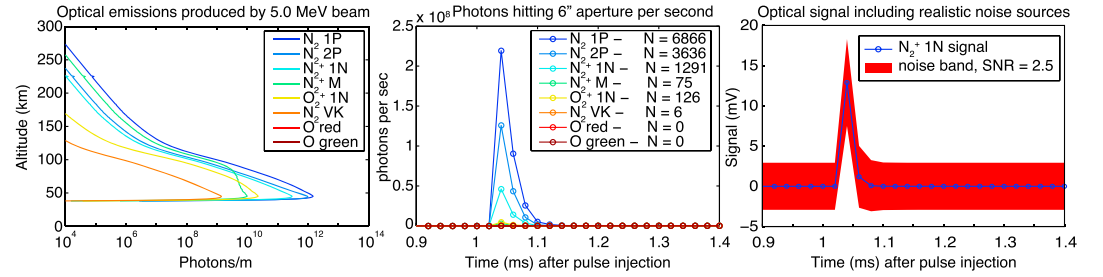


Figure 7. Optical emissions for 5 MeV beam. (left) Altitude profiles of optical emissions, integrated in time. (middle) Pulse of optical photons versus time, measured on the ground. The values of N in the legend denote the total photons measured by a 15 cm aperture over the duration of the pulse. (right) Pulse measured in the 3914 Å line of N_2^+ 1N, and a simulated noise band to show the estimated signal-to-noise ratio.

radial distance, from Figure 6 we see that the flux is significantly reduced. A planned experiment will have to take the backscattered beam size into account and compare it to the velocity and altitude of the injector/detector platform.

4.4. Optical Emissions

Optical emissions were observed during the SEPAC keV beam experiment flown on the ATLAS-1 shuttle mission. *Neubert et al.* [1995] measured emission brightness as high as 5 kR, higher than model estimates of 1 kR; the higher emissions were attributed to excitation by suprathermal electrons, the result of wave-particle interactions. That experiment used a 6.25 keV beam with 1.2 A current.

For optical emissions in our simulated MeV beam (Figure 3, O2), emission rates are calculated from the secondary ionization profiles. We follow the method outlined in *Lehtinen et al.* [1997] and *Marshall et al.* [2010] to compute optical excitation rates. The method uses a generic excitation cross section given by [Vallance Jones, 1974, p. 92]

$$\sigma(E) = \frac{\sigma_{\max} E_{\max}^2 (E - I)}{E(E_{\max}(E_{\max} - 2I) + EI)} \quad (5)$$

where σ_{\max} is the maximum cross section, E_{\max} is the energy at which that maximum is attained, and I is the ionization potential; σ_{\max} and E_{\max} are taken from Vallance Jones [1974] and I is taken from Rees [1992]. The numeric values of these quantities are tabulated in Marshall et al. [2010]. The production rates of individual ions and excited states are calculated from the total ionization cross section using equations (4.2.1) (f–l) of Vallance Jones [1974, p. 105].

From production rates r , we evaluate the number density of excited molecules through a simple chemistry model. For example, the evolution of the N_2B state (which emits the N_2 1P band system) is governed by

$$\frac{dN_{N_2B}}{dt} = \underbrace{r_{N_2B}}_{\text{excitation}} + \underbrace{a_{N_2C}N_{N_2C}}_{\text{cascading from } N_2C} - \underbrace{a_{N_2B}N_{N_2B}}_{\text{spontaneous emission}} - \underbrace{k_{N_2B,N_2}N_{N_2B}N_{N_2}}_{\text{quenching with } N_2} \quad (6)$$

where a_X is the rate constant for state X , k_{N_2B,N_2} is the quenching rate of the N_2B state with N_2 , and r_{N_2B} is the excitation rate of the N_2 B state. We solve this equation with a simple implicit Euler scheme to guarantee stability; apart from cascading terms, the equations for the different species of interest are uncoupled. The number of photons emitted per m³/s is then given by $\gamma_{N_2 1P} = N_{N_2B}a_{N_2B}$.

We calculate emission rates for N_2 first positive (1P) as above, N_2 2P, N_2 Vegard-Kaplan (VK), N_2^+ First Negative (1N), N_2^+ Meinel (M), O_2^+ 1N, $O(^1S)$ green line (557.7 nm), and $O(^1D)$ red line (630.0 nm). Rate constants a and quenching rates k are taken from Vallance Jones [1974, p. 119].

Figure 7a shows the time-integrated emissions for the 5 MeV, 0.1 A beam. Similar to the electron density perturbation, the optical emissions peak sharply at just below 50 km altitude. The brightest emission is the N_2 1P band system, followed closely by N_2 2P and N_2^+ 1N. The N_2 VK system is very weak, despite the strong cross section of the N_2 $A^3\Sigma$ state, because this metastable state has a lifetime of ~ 2 s. Similarly, the red and green line forbidden emissions of atomic oxygen do not even show up on this plot, due to

their 110 and 0.7 s lifetimes, respectively, and due to the fact that O density is negligible below 90 km altitude. As such, these latter three emissions are not likely to be valuable in the diagnostics of the beam-atmosphere interaction.

To estimate the expected signature on the ground, we propagate photons from their emission location to a detector at the footprint of the magnetic field line (i.e., looking up the field line), including appropriate time delays. The optical pulse that would be detected by a 15 cm aperture system (with a field of view encompassing the ~ 200 m radius emitting column) is shown in Figure 7b. Photons arrive at the detector about 1 ms after the beam was injected from 300 km altitude, as expected, and are “bunched” into a very narrow pulse due to the fact that the beam and the photons are propagating in the same direction for this detector scenario. A detector side viewing the column would see a broader pulse. The legend shows the total number of photons that would enter the 15 cm aperture (N). The dominant emissions are again the N_2 1P, N_2 2P, and N_2^+ 1N systems.

To assess detectability, we can estimate the SNR for a realistic optical system. We use parameters for a Hamamatsu H10493 photomultiplier tube, outfitted with a 30 Å narrowband filter around the 3914 Å line of the N_2^+ 1N system. Accounting for shot noise on the signal and the background sky (with spectral brightness estimated from *Broadfoot and Kendall* [1968]), dark noise in the photomultiplier tube, amplifier noise with 50 kHz bandwidth, and digitizer noise, we compute the SNR and plot the “noise band” on top of the expected signal in Figure 7c. For this 5 MeV, 0.1 A, 0.1 μ s pulse, we expect an SNR in the 3914 Å line of ~ 2.5 . Figure 7 (right) shows what this SNR would look like in real data and shows that it is likely detectable. Note that the noise is dominated by shot noise on the signal; hence, this SNR can only be improved with a larger aperture system.

4.5. X-rays

While the energy spectrum of energetic photons produced in this work crosses the boundary between X-rays and gamma rays, we refer to all energetic photons as X-rays for simplicity. Referring to Figure 3, the calculation of X-ray production and propagation requires two steps. First, using the electron distributions at well-refined time steps, we calculate the production of X-rays from the bremsstrahlung cross section using the method of *Lehtinen* [2000]. The doubly differential cross section is approximated by two independent terms, one which describes the cross section per unit energy (i.e., energy scattering), and other describes the cross section per unit solid angle (i.e., angular scattering). Ultimately, the cross section relates the input electron momentum \mathbf{p} to the output electron momentum \mathbf{p}' , the output photon energy k , and the scattering angle θ . The details of the computation of the photon production can be found in *Lehtinen* [2000]. For our 5 MeV beam, we find that 2.83% of the total input electron energy is converted to X-ray photons over the duration of the pulse; this compares favorably with *Krause* [1998, Figure 2.21], where for the 5 MeV beam just over 2% of the beam energy is lost to bremsstrahlung.

This computation results in a distribution of some large number of photons (say, 50,000) with positions specified by the positions of the electrons, and momentum components derived from the electron momentum components, photon energies, and scattering angles. This distribution of photon \mathbf{q} and \mathbf{p} are then propagated through the SMC code, with a flag to note that the particles are photons. This flag disables dynamic friction and angular scattering, and enables the photoelectric effect and Compton scattering. Pair production is not considered, since the number of electron-positron pairs is expected to be negligibly small for electrons with $\epsilon \leq 10$ MeV.

Simulations show that X-rays are primarily produced with energies in the tens to hundreds of keV for these MeV beams, and primarily propagating in a beam-like configuration downward, in the same direction as the electrons (i.e., small scattering angles). However, due to the increasingly dense atmosphere, no photons reach the ground, and multiple scattering events result in a scattered photon distribution that is roughly isotropic in the upper hemisphere direction. As such, X-rays could only be detected on a high-altitude platform, such as an upward looking balloon or a downward looking rocket or spacecraft, including the injection platform itself.

Figure 8 shows the results of the X-ray calculations for the 5 MeV, 0.1 A beam. The top row shows results for X-ray detection on a high-altitude platform at 500 km; the bottom row shows detection on a platform at 40 km altitude, such as a balloon, directly below the interaction region. Figure 8 (left) shows the X-ray pulse as a function of time, averaged inside a 300 km radius (top) or 10 km radius (bottom). The pulse of photons

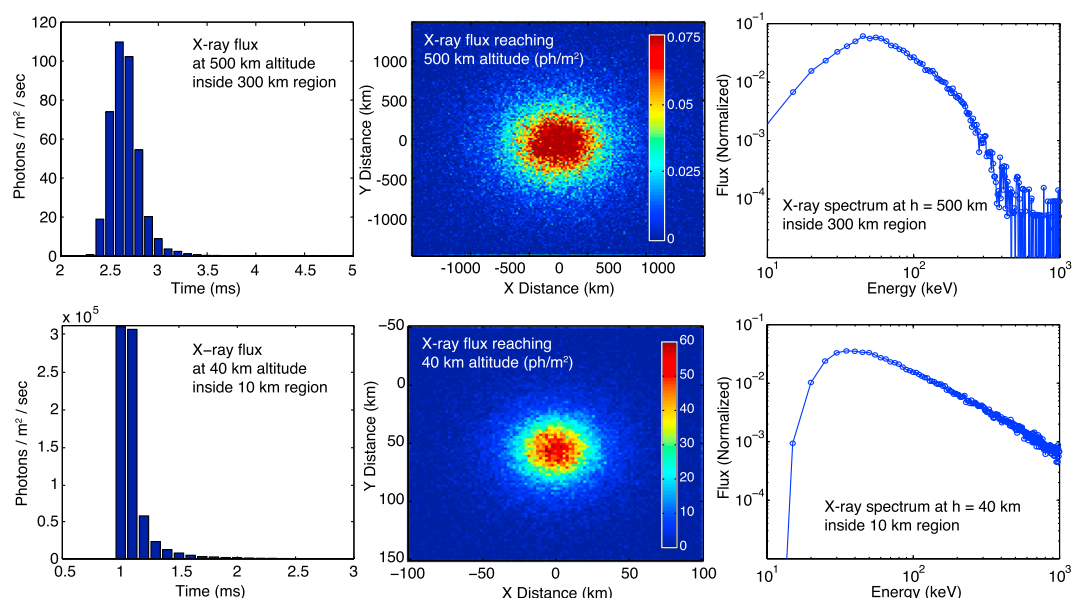


Figure 8. X-ray production from 5 MeV beam. (top row) X-rays measured at 500 km, i.e., backscattered. (bottom row) X-rays measured at 40 km altitude, below the interaction region. (left) Pulse of photons versus time at measurement location. (middle) Time-integrated X-ray flux in 2-D space at measurement altitude. (right) Spectrum of X-rays at measurement altitude.

lasts about 0.5 ms. Figure 8 (middle) shows the time-integrated photon flux in a 2-D histogram, in units of photons/m². We note that as expected, at 500 km photons are spread over a very large area, and so the flux is very small, with a peak of ~0.05 photons/m². However, at 40 km (Figure 8, bottom row, middle) the flux is considerably higher, reaching 60 photons/m², and concentrated in a 20 km wide region. Figure 8 (right) shows the X-ray spectrum. At 500 km the spectrum is hard below ~50 keV and soft above this energy. Very few photons are detected with energies above ~300 keV. At 40 km altitude, the downgoing X-ray spectrum shows fewer low-energy X-rays and more high-energy X-rays; this spectrum is closer to the generated X-ray spectrum since it has not undergone significant atmospheric absorption and scattering yet.

X-ray fluxes were also calculated by *Berger and Seltzer* [1972] and by *Krause* [1998] using a similar bremsstrahlung cross section. Similar to our results, at low-Earth orbit (LEO) altitudes these authors found a photon spectrum with a peak around 50–60 keV. They also showed that the reduced low-energy flux is due to atmospheric attenuation. Similarly, for balloon altitudes, *Krause* [1998] found a peak in the X-ray flux at 30–40 keV, similar to our results.

A major difference between our results and those of *Krause* [1998] is that we do not find a “null” in the backscattered direction. *Krause* [1998] showed that the flux increases with a radial displacement of 0 to ~60 km from the backscattered direction. In our results, the backscattered flux is flat from 0 to ~200 km in the radial direction (at 500 km altitude). *Krause* [1998] attributes the “null” to the preferential bremsstrahlung scattering in the forward direction. However, in reality photons undergo a large number of scattering events before escaping the atmosphere, and thus the flux becomes more isotropic (except for attenuation, dependent at atmospheric path length). These multiple scatterings are inherently included in our Monte Carlo simulation, but not in the analytical model of *Krause* [1998].

In the next section we explore different injection energies and divergence and see the effect on the various diagnostics. In section 6 we investigate alternative injection scenarios, such as a lower altitude rocket or balloon injection.

5. Variation in Beam Energy and Divergence

In this section we investigate the effects of beam energy and divergence on the detectable diagnostics. The COMPASS instrument will have the ability to vary the output beam energy and divergence; finding the most

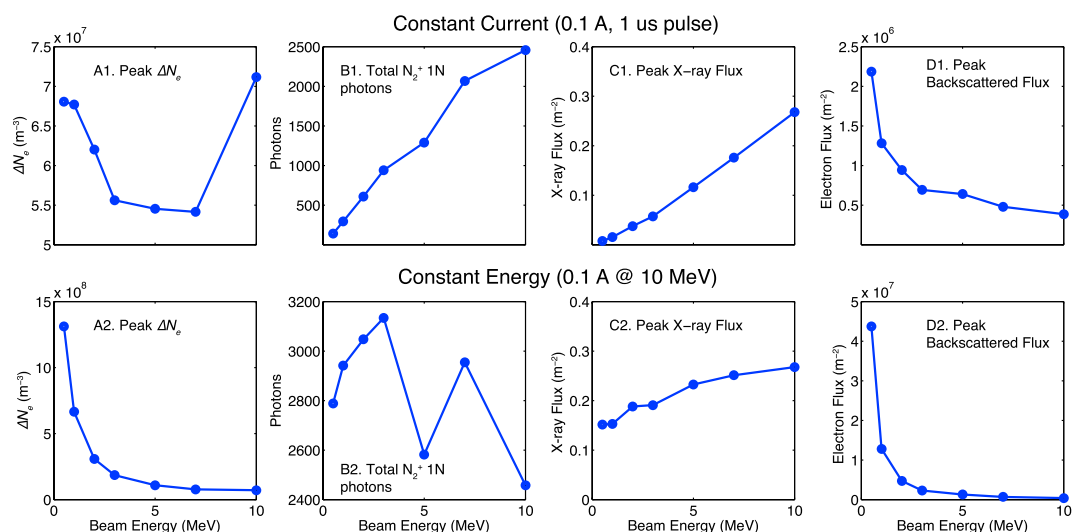


Figure 9. Variation in signatures with beam electron energy, for (a1–d1) constant beam current and (a2–d2) constant beam energy.

practical and scientifically useful parameters is a primary goal of this study. Note that we do not need to vary the input current and pulse length: other than the modified electron density, which involves chemistry, each of the diagnostics is linearly proportional to the total number of electrons injected.

5.1. Beam Energy

We vary the beam energy from as low as 0.5 MeV to as high as 10 MeV. Figures 9a1–9d1 (top row) shows the variation in diagnostic signatures (electron density change, optical signature, X-ray flux measured at LEO altitudes, and backscattered electron flux) with beam energy, while holding the beam current and pulse length constant. This implies that the beam peak power increases with energy, and the total energy injected also increases.

We observe from Figure 9a1 that the peak change in electron density is only weakly dependent on beam energy. This counterintuitive result can be explained by referring to Table 2: the equilibrium beam radius assumed increases with energy, so while the total ionization increases with beam energy, it is spread over a larger cross-section area. Thus, the effects of increased total ionization and increased beam radius cause the electron density to be roughly the same across beam energy.

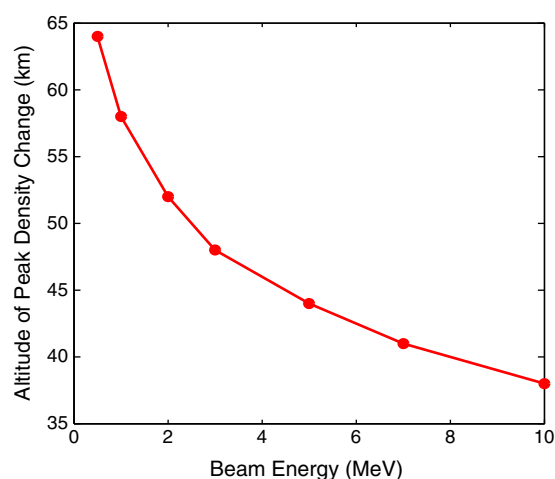


Figure 10. Peak altitude of ionization for different beam energies. Lower energy electrons do not penetrate as far into the atmosphere due to higher angular scattering.

Figures 9b1 and 9c1 show that the total optical photons produced (we compare $N_2^+ 1N$ since it is the most likely to be detected from the ground) and the total LEO X-ray photons increase with beam energy, integrated over the time duration of the pulse. This is not at all surprising; more total energy input into the system leads to more photons produced.

Figure 9d1 shows that the peak time-integrated backscattered electron flux decreases with beam energy. This dependence is explained by the angular scattering cross sections, which decrease with energy. Hence, lower energy electrons undergo wider-angle scattering events and are more likely to be turned around before losing all of their energy. This is similarly reflected by the altitude of deposition: Figure 10 shows the altitude of the peak in electron density change.

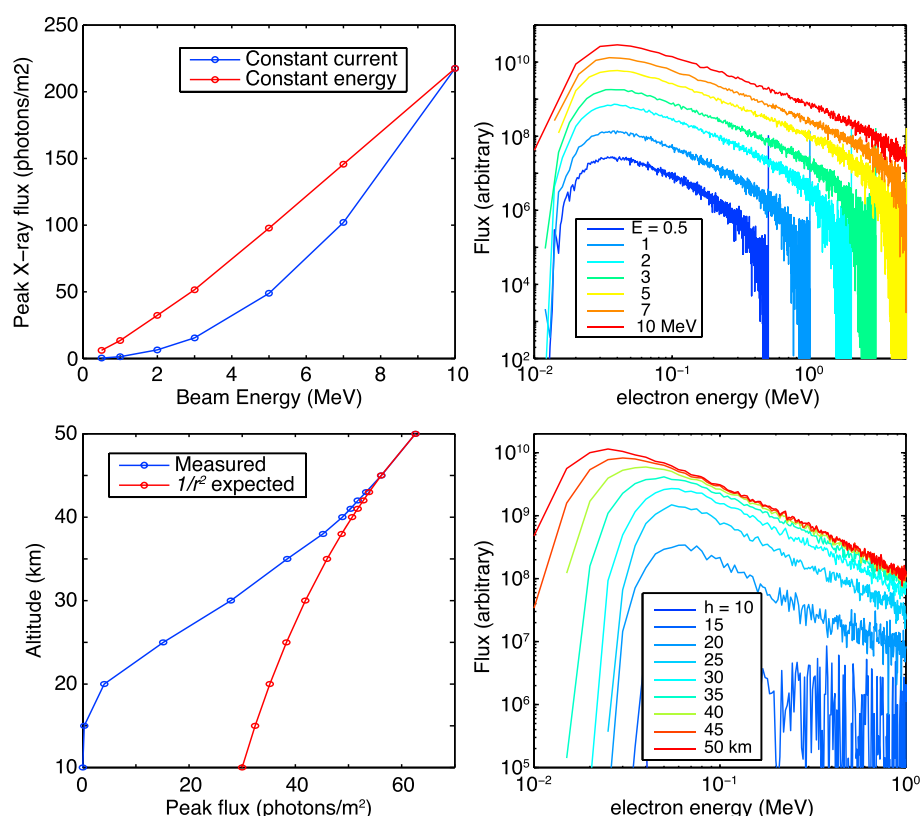


Figure 11. X-ray flux measured at balloon altitudes. (top left) Peak X-ray flux measured at 40 km altitude for different energy beams, for both constant energy and constant current beams. (top right) X-ray spectrum measured for each beam energy. (bottom left) Peak X-ray flux measured at different altitudes for a 5 MeV electron beam. (bottom right) Spectrum of X-rays measured at each altitude.

Lower energy electrons do not penetrate as deep into the atmosphere as higher-energy electrons, and thus are more likely to reverse direction and escape back up the field line.

While the COMPASS instrument may be able to increase the beam energy, it is more likely that it will do so with a reduction in output current. To better compare different beam energies, we can rescale the outputs so that we compare constant total beam energy. The only output that cannot be directly scaled is the electron density; we rescale the ionization results, but rerun the GPI chemistry code to calculate the resulting electron density change.

Figures 9a2–9d2 (bottom row) show the same comparisons as Figure 9, but for constant total beam energy. In this case, we observe the following:

1. The peak electron density change (Figure 9a2) is significantly higher for the lower energy beam, for the reasons described above. This again implies that a lower energy beam will have a stronger radar signature.
2. The optical signature does not vary significantly with beam energy. For the same total input electron energy, roughly the same number of optical photons are produced. More electrons are produced for lower energy beams: we speculate that this is due to the higher interaction altitude, where quenching is reduced.
3. The X-ray flux measured at LEO also does not have significant variation with beam energy (less than a factor of 2, while the beam energy varies by a factor of 20). For the same total input electron energy, roughly the same number of X-rays will be produced.
4. The backscattered flux (Figure 9d2) is also significantly higher for lower energy beams, again for the same reasons described above.

In Figure 11, we investigate the effects of different beam energies on the downgoing X-ray flux. The top left plot shows the peak X-ray flux (time integrated) measured at 40 km altitude for different beam energies, both for the constant current (0.1 A) and constant energy cases. Clearly, higher-energy electron beams

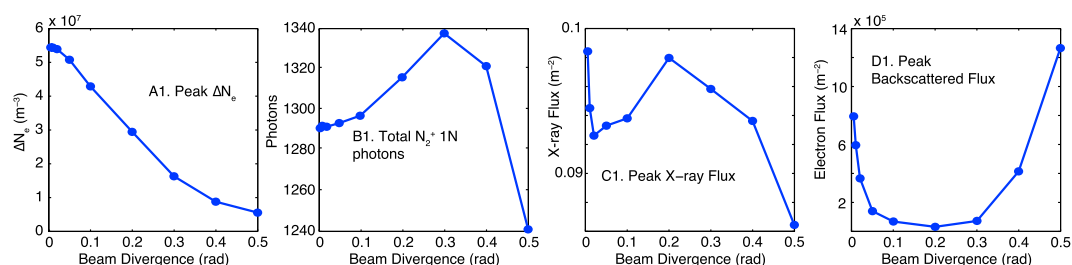


Figure 12. Variation in signatures with beam divergence angle. Panels are identical to the top row of Figure 9.

produce greater X-ray flux, even when controlling for the beam total energy. The top right plot shows the spectra of photons produced by each beam. The shape of the spectrum is similar for each beam, and the peak in the photons spectrum is always around 30–40 keV.

Figure 8 (bottom left) demonstrates the attenuation of the X-ray flux from the 5 MeV beam as it propagates downward. There is a rapid dropoff in the X-ray flux below 40 km altitude, and essentially, no photons reach below 10 km. The red curve is a $1/r^2$ fit to the blue curve, assuming no attenuation occurs between 50 and 45 km altitude; the fit works when the X-ray source is assumed near ~ 140 km. This simply demonstrates that the reduction of the X-ray flux is primarily due to attenuation and scattering, and not due to the spread of photons over distance. Figure 8 (bottom right) shows the spectrum measured at each altitude. Clearly, all photon energies are attenuated/scattered for the downgoing photon beam, but lower energy electrons are lost more rapidly, so that the measured peak in the spectrum moves to higher energies at lower altitudes.

5.2. Beam Divergence

Next we vary the input beam divergence angle θ from 0.005 radians (0.29°) to 0.5 radians (28.6°). The associated pitch angle distributions have peaks at these divergence angles. Note that injections with divergence angles larger than even 0.05 radians are not realistic; we include them here in order to investigate the effects on diagnostics in order to verify our interpretation of results. Figure 12 shows the resulting diagnostic signatures, similar to Figure 9 for energy, as a function of the divergence angle. We observe the following:

1. The peak electron density disturbance, ΔN_e , decreases with θ . Referring to Figure 4, this is simply due to the fact that the beam radius increases with divergence angle, roughly linearly. Hence, we would expect the ionization density to decrease as the square of θ . At the same time, we find that the altitude of the peak electron density change is not affected and is found to be within 1 km of 44 km altitude for all of these beams.
2. The total photon production, both optical and LEO X-ray, is very weakly affected by the beam divergence. Essentially, the same total energy is being deposited in the same altitude range, so we expect roughly the same photon production.
3. The backscattered flux decreases with θ , for the same reason as the electron density: the backscattered beam has a larger radius for larger θ . In fact, we find that the total backscattered energy increases with θ , very weakly for $\theta < 0.1$ and then very rapidly for $\theta > 0.1$. The total backscattered energy for $\theta = 0.1$ and 0.5 radians is 1.3 and 150 times the backscattered energy for $\theta = 0.01$ radians, respectively. This explains the increase in backscattered flux for higher θ in Figure 12.

In summary, we find that for the same total beam energy, higher energy electron beams produce weaker electron density perturbations and lower backscattered fluxes, due to the increased beam radius, while the optical fluxes are mostly unaffected. Higher beam divergence has the same effects on all four diagnostics, except very high divergences can result in higher backscattered fluxes.

6. Other Injection Scenarios

In this section we briefly investigate and compare the results of injections from lower altitudes. In particular, a low-cost rocket could inject the beam from, say, 80 km, without significant degradation of the signatures and potentially with better detection of diagnostic signatures. Second, a balloon injection from 40 km may provide the lowest-cost scenario for first experiments. In both cases, there is significant atmosphere

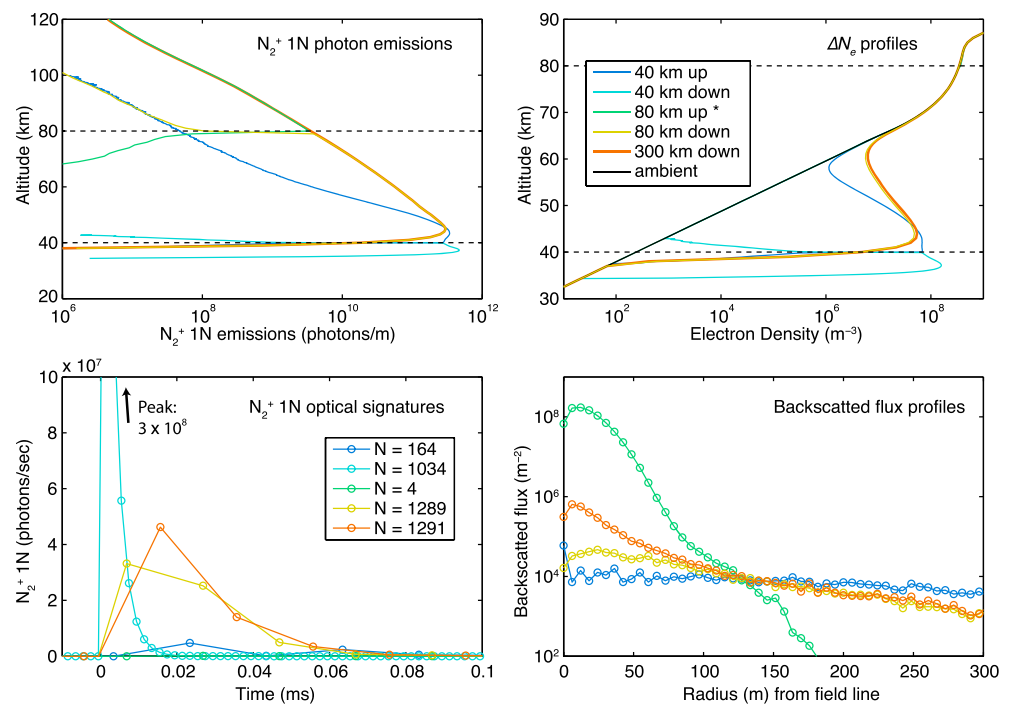


Figure 13. Injection scenarios from 80 and 40 km altitudes; the legend is shown in the top right and applies to all panels. (top left) N_2^+ 1N emissions versus altitude. Dashed black lines show the injection altitudes. (bottom left) Expected optical pulse on the ground; recall that N denotes the total photons reaching the 15 cm aperture detector on the ground. (top right) Perturbed electron density profiles along the beam axis. Note that no perturbation is visible for the 80 km upward injection. (bottom right) Backscattered flux versus radial distance.

above the injection altitude, opening up the possibility of injections both downward, toward the Earth, and upward, away from the Earth.

For the 80 km altitude injection, we use the same parameters as previous simulations, except that the initial electron $q_z = 80$ km. For the 40 km injection, we find that a more highly resolved altitude profile and time steps are required to observe the evolution of the beam. As such the altitude spacing is decreased from 1 km to 100 m, and the output time step is reduced from 20 μ s to 2 μ s.

Figure 13 compares the results of five injections: (i) the standard 300 km downward injection (300 km down), (ii) injection from 80 km downward and (iii) upward, and (iv) 40 km injection downward and (v) upward. Figure 13 (top left) shows the optical emission profiles versus altitude for the N_2^+ 1N emission. Figure 13 (bottom left) shows the expected optical pulse on the ground, assuming the same 15 cm optical aperture as earlier; in this case, however, the time axis has been shifted to account for the different delays from each pulse injection altitude. Figure 13 (top right) shows the peak electron density perturbation, along the beam axis, as a function of altitude. Figure 13 (bottom right) shows the backscattered electron flux as a function of radial distance from the field line. We will analyze these results one injection scenario at a time and compare them to the 300 km injection scenario that has been our baseline throughout this paper.

Eighty kilometers downward injection: In this scenario, the optical emissions show that the vast majority of ionization and emissions are produced between 40 and 80 km. The emission and electron density profiles otherwise match that of the 300 km injection very closely. The peak electron density perturbation at 44 km is $0.48 \times 10^8 \text{ m}^{-3}$, compared to $0.55 \times 10^8 \text{ m}^{-3}$ for the 300 km injection. The optical pulse is very similar to that of the 300 km injection; the difference is likely due to a binning effect (the time histogram bin edges are not the same for both simulations). The backscattered flux, however, appears somewhat lower for the 80 km case. In fact, while for the 300 km injection, 0.042% of the total electron energy is backscattered, in the 80 km case, 0.034% is backscattered, only fractionally less. While it is not shown visually, we have also compared the X-ray flux for these different injection scenarios; we find that the 80 km downward injection has a peak X-ray flux at 500 km altitude of 0.095 photons/ m^2 , compared to 0.116 photons/ m^2 for the 300 km

injection. Overall, we see that the 80 km injection compares favorably to the 300 km injection, providing strong support for a lower altitude rocket experiment to study the beam-atmosphere interaction.

Forty kilometers downward injection. In this case, optical emissions are produced primarily below 40 km altitude, and the electron density is perturbed below 40 km, despite the fact that the usual peak for a 5 MeV beam is at 44 km altitude. Essentially, electrons are being dumped out of the accelerator and they immediately disperse into the atmosphere through collisions. Most of the energy is deposited between 37 and 40 km. Interestingly, the peak electron density change is higher than the other cases ($1.58 \times 10^8 \text{ m}^{-3}$ compared to $0.55 \times 10^8 \text{ m}^{-3}$ for the 300 km injection); this is due to the fact that the energy is deposited over a very narrow altitude range. The optical pulse received at the ground (Figure 13, bottom left) is very intense, but short duration; the total number of photons is actually 20% less than the 300 km and 80 km downward injections. Also of note, not a single electron in the simulation of 10^6 electrons is backscattered; hence, there is no light blue line in Figure 13 (bottom right). The peak X-ray flux at 500 km is $\sim 0.063 \text{ photons/m}^2$, about half that of the 300 km injection. Overall, we see that this injection scenario also compares favorably to the 300 km and 80 km injections, except that there is no backscattered electron signature.

Forty kilometers upward injection. This scenario aims to perturb the atmosphere by injection from below. We see that the optical emissions compare closely to the 80 km and 300 km downward injections, but fewer photons are produced at higher altitudes, since few survive the traverse. The electron density profile (Figure 13, top right) shows a strong response between 40 and 50 km, with a weaker response between 50 and 70 km compared to the 300 km injection. The peak electron density perturbation is $0.69 \times 10^8 \text{ m}^{-3}$, slightly higher than the 300 km case, but only half that of the 40 km downward injection. The optical pulse is very weak, and only $\sim 13\%$ as many photons reach the detector on the ground. This is due to the fact that the emitting region is thinner in altitude, and the optical detector integrates along the field line. We see that for the 40 km upward injection, a similar total energy is “backscattered” (0.043% of the input energy), i.e., escapes to 500 km altitude, but many fewer total electrons; the backscattered electron distribution is primarily made up of $\sim 5 \text{ MeV}$ electrons that made it through the atmosphere without scattering many times and are found in a very narrow radius, meaning they are primarily field aligned. Finally, the peak X-ray flux produced by this beam is $\sim 0.2 \text{ photons/m}^2$, about twice that of the other injection scenarios. In summary, this injection scenario produces a strong electron density perturbation, and may produce a stronger X-ray response, but is not ideal for optical emissions or backscattered electrons.

Eighty kilometers upward injection: This scenario is investigated to study the effect of the upper atmosphere on the beam and to see how well it escapes into the magnetosphere for other experiments such as field-line tracing. We find that the optical emission profile follows the 300 km injection profile for altitudes above 80 km, and only a few photons are produced below 80 km. The total photons reaching the ground are very few, and there is no observable electron density perturbation. The “backscattered” electron flux is very high, and reflects the beam radius very closely. In fact, 99.7% of the beam energy escapes to 500 km altitude (not accounting for losses due to spacecraft charging or wave-particle interactions), and slightly more electrons escape, thanks to a few secondary energetic electrons produced with small scattering angles. In short, an injection from 80 km will easily escape into the magnetosphere, nearly unperturbed by the atmosphere; but an injection from 40 km altitude will not fare nearly as well.

7. Summary

We have presented results of a series of Monte Carlo simulations of a beam of energetic (MeV) electrons impinging on the Earth's atmosphere from above and in a few cases from below. Our model propagates electrons through the atmosphere, taking into account energy losses due to dynamic friction and scattering through angular diffusion. Energy deposition is calculated from dynamic friction and used to estimate new ionization and optical emissions produced. A five-species chemistry model is used to calculate the perturbed electron density from the ionization profiles. Finally, X-ray production is calculated from the bremsstrahlung cross section, and then X-ray photons are propagated through the atmosphere taking into account Compton scattering and the photoelectric effect.

These model calculations are used to estimate the diagnostic signatures of the beam, including electron density perturbations, optical emissions, X-ray fluxes, and backscattered electron fluxes. We simulate a canonical 5 MeV, 0.1 A, 1 μs pulse of electrons and find that (a) the electron density perturbation reaches a peak of $0.55 \times 10^8 \text{ m}^{-3}$ at 44 km altitude; (b) the time-integrated backscattered flux is $> 6 \times 10^5 \text{ m}^{-2}$ and

primarily consists of 20 keV up to a few hundred keV electrons; (c) optical emissions are weak, but potentially detectable from the ground; and (d) X-ray fluxes are weak, amounting to just over 1 photon/m², even when time integrated and measured at 100 km altitude. Of course, the X-ray flux will be much higher closer to the source; a balloon flying close to the interaction region at 44 km altitude will likely measure a large number of photons. Furthermore, each of the outputs scales directly with current and pulse time, i.e., with total injected electrons; so a larger or longer current pulse will produce proportionally stronger signatures.

We compare simulations with different beam energies and divergence angles. We find that for a constant current (0.1 A) pulse, higher beam energies result in higher optical and X-ray emissions, but lower backscattered fluxes. When the beam is adjusted to have constant total energy, we observe that the optical and X-ray fluxes are weakly dependent on the electron energy, but the backscattered fluxes and electron density perturbation are much stronger for lower energy beams. Similarly, we find that a lower beam divergence angle produces stronger electron density perturbations and backscattered fluxes but has little effect on the optical and X-ray fluxes. The exception occurs for very high divergence angles > 0.2 radians, for which the backscattered fluxes increase with divergence angle.

Finally, we investigate different injection scenarios, including upward and downward injections from 40 to 80 km altitudes. We observe that for downward injections, both of these scenarios produce signatures similar to the higher-altitude 300 km injection, except that the 40 km downward injection has no backscattered electrons. For the upward injections, the 40 km case produces significant signatures, but the 80 km beam essentially escapes the atmosphere unperturbed; this is not surprising since the strongest interaction region for these electron energies is around 44 km.

Overall, we find that a 0.1 A, 1 μ s pulse of electrons, from 0.5 MeV up to 10 MeV, will produce significant and detectable signatures. These results will help to drive the design of a low-cost, low-power electron accelerator structure that can be flown on a high-altitude platform.

Acknowledgments

This work was supported by NSF INSPIRE award 1344303. The Monte Carlo model and analysis codes used to produce the results in this paper are available upon request from the author.

Michael Liemohn thanks Torsten Neubert and Evgeny Mishin for their assistance in evaluating this paper.

References

- Banks, P. M., A. C. Fraser-Smith, B. E. Gilchrist, K. J. Harker, L. R. O. Storey, and P. R. Williamson (1987), New concepts in ionospheric modification, *Final Rep. AFGL-TR-88-0133*, Stanford Univ., Air Force Geophys. Lab., Bedford, Mass.
- Banks, P. M., A. C. Fraser-Smith, and B. E. Gilchrist (1990), Ionospheric modification using relativistic electron beams, *AGARD Conf. Proc.*, 485, 22-1-22-18.
- Berger, M. J., and S. M. Seltzer (1972), Bremsstrahlung in the atmosphere, *J. Atmos. Terr. Phys.*, 34(1), 85-108.
- Broadfoot, A. L., and K. R. Kendall (1968), The airglow spectrum, 3100-10,000 Å, *J. Geophys. Res.*, 73, 426-428.
- Burch, J. L., S. B. Mende, N. Kawashima, W. T. Roberts, W. W. L. Taylor, T. Neubert, W. C. Gibson, J. A. Marshall, and G. R. Swenson (1993), Artificial auroras in the upper atmosphere. 1. Electron beam injections, *Geophys. Res. Lett.*, 20(6), 491-494.
- Glukhov, V. S., V. P. Pasko, and U. S. Inan (1992), Relaxation of transient lower ionospheric disturbances caused by lightning-whistler-induced electron precipitation bursts, *J. Geophys. Res.*, 97(A11), 16,971-16,979.
- Hedin, A. E. (1991), Extension of the MSIS thermospheric model into the middle and lower atmosphere, *J. Geophys. Res.*, 96(A2), 1159-1172, doi:10.1029/90JA02125.
- Humphries, S. (1990), *Charged Particle Beams*, John Wiley, New York.
- Krause, L. H. (1998), The interaction of relativistic electron beams with the near-Earth space environment, PhD thesis, Univ. of Michigan, Ann Arbor, Mich.
- Lehtinen, N. G. (2000), Relativistic runaway electrons above thunderstorms, PhD thesis, Stanford Univ., Stanford, Calif.
- Lehtinen, N. G., and U. S. Inan (2007), Possible persistent ionization caused by giant blue jets, *Geophys. Res. Lett.*, 34, L08804, doi:10.1029/2006GL029051.
- Lehtinen, N. G., T. F. Bell, V. P. Pasko, and U. S. Inan (1997), A two-dimensional model of runaway electron beams driven by quasi-electrostatic thundercloud fields, *Geophys. Res. Lett.*, 24(21), 2639-2642.
- Lehtinen, N. G., T. F. Bell, and U. S. Inan (1999), Monte Carlo simulation of runaway MeV electron breakdown with application to red sprites and terrestrial gamma ray flashes, *J. Geophys. Res.*, 104(A11), 24,699-24,712.
- Marshall, R. A., R. T. Newsome, N. G. Lehtinen, N. Lavassar, and U. S. Inan (2010), Optical signatures of radiation belt electron precipitation induced by ground-based VLF transmitters, *J. Geophys. Res.*, 115, A08206, doi:10.1029/2010JA015394.
- Mishin, E. V., and G. V. Khazanov (2006), Tether-induced airglow: Collisionless effects, *Geophys. Res. Lett.*, 33, L15015, doi:10.1029/2006GL026220.
- Neubert, T., and P. M. Banks (1992), Recent results from studies of electron beam phenomena in space plasmas, *Planet. Space Sci.*, 40(2/3), 153-183.
- Neubert, T., and B. E. Gilchrist (2002), Particle simulations of relativistic electron beam injection from spacecraft, *J. Geophys. Res.*, 107(A8), 1167, doi:10.1029/2001JA900102.
- Neubert, T., and B. E. Gilchrist (2004), Relativistic electron beam injection from spacecraft: Performance and applications, *Adv. Space Res.*, 34(11), 2409-2412.
- Neubert, T., W. W. L. Taylor, L. R. Storey, N. Kawashima, W. T. Roberts, D.-L. Reasoner, P. M. Banks, D. A. Gumett, R. L. Williams, and J. L. Burch (1986), Waves generated during electron beam emissions from the space shuttle, *J. Geophys. Res.*, 91(A10), 11,321-11,329.
- Neubert, T., P. M. Banks, B. E. Gilchrist, A. C. Fraser-Smith, and P. R. Williamson (1990), The interaction of an artificial electron beam with the Earth's upper atmosphere: Effects on spacecraft charging and the near-plasma environment, *J. Geophys. Res.*, 95(A8), 12,209-12,217.
- Neubert, T., J. L. Burch, and S. B. Mende (1995), The SEPAC artificial aurora, *Geophys. Res. Lett.*, 22(18), 2469-2472.

- Neubert, T., B. Gilchrist, S. Wilderman, L. Habash, and H. J. Wang (1996), Relativistic electron beam propagation in the Earth's atmosphere: Modeling results, *Geophys. Res. Lett.*, *23*(9), 1009–1012.
- Neupert, W. M., et al. (1982), Science on the space shuttle, *Nature*, *296*, 193–197.
- Rees, M. H. (1963), Auroral ionization and excitation by incident energetic electrons, *Planet. Space Sci.*, *11*(10), 1209–1218.
- Rees, M. H. (1992), Auroral energy deposition rate, *Planet. Space Sci.*, *40*(2/3), 299–313.
- Stone, N. H., and C. Bonifazi (1998), The TSS-1R mission: Overview and scientific context, *Geophys. Res. Lett.*, *25*(4), 409–412.
- Vallance Jones, A. (1974), *Aurora*, Reidel, Boston, Mass.
- Winckler, J. R. (1980), The application of artificial electron beams to magnetospheric research, *Rev. Geophys.*, *18*(3), 659–682.